Influence of the Perception, Observer Position, and Broadband Self-Noise on Low-Fidelity UAM Vehicle Perception-Influenced-Design (PID) Optimization

Leonard V. Lopes*
NASA Langley Research Center, Aeroacoustics Branch
Hampton, VA

Daniel J. Ingraham
NASA Glenn Research Center, Acoustics Branch
Cleveland, OH

ABSTRACT

This paper will present an approach in design optimization of a proprotor in a forward flight condition with several acoustic objective functions that simulate community response. An adjoint-capable blade element momentum theory (BEMT), implemented in CCBlade.jl, will be used to compute the blade forces and inflow properties required to compute tonal and broadband noise using the second-generation Aircraft NOise Prediction Program (ANOPP2). The influence of broadband noise, observer location, and choice of perception constraint on optimized values of rotation rate, chord distribution, and twist angle will be shown. It is determined that broadband self-noise is an influential source noise mechanism in the design optimization when frequency weighting is used to predict the noise at an out-of-plane observer position.

NOTATION

English:

c_∞	speed of sound, m/s
c	blade section chord, in
$\mathscr{C}$	monopole radiation coefficient, $m^{-1}s^{-2}$
dB	decibel, ref: 20 μ Pa, dB
D	proprotor diameter, in
$\mathscr{D}, \mathscr{E}$	dipole radiation coefficients, m^{-1} $m^{-1}s^{-1}$
f	integration surface defined by $f = 0$
F	integration line (quarter chord)
$\boldsymbol{F}$	blade section force, N/m
h	trailing edge bluntness, in
H	Heaviside function
K	blade section spanwise length, m
$\boldsymbol{L}$	dipole source term, $kgm^{-1}s^{-2}$
$\mathbb{L}$	perception constraint, dB or dBA
M	Mach number
p	pressure, Pa
P	proprotor pitch, in
Q	monopole source strength, $kgm^{-1}s^{-2}$
r	radial location on blade, in
R	blade radius, in
t	observer time, sec
T	proprotor thrust, lbs
$\boldsymbol{T}$	Lightill stress tensor, $kgm^{-1}s^{-2}$
u	time-independent coordinate
v	velocity, m/s
$\boldsymbol{x}$	spatial location, m
$\boldsymbol{y}$	blade section spatial location, m

Greek:

α	effective angle of attack, rad
δ	Dirac delta function
δ	boundary layer thickness, in
η	proprotor efficiency
λ	induced inflow velocity, m/s
ρ	density, kgm^{-3}
τ	retarded time, s
ϕ	blade twist, rad
Ψ	cross-sectional area, m^2
ω	proprotor rotation rate, rad/s

Subscript:

x_{1A}	Formulation 1A
x_d	dipole
x_{hub}	hub quantity
x_k	blade section index
x_m	monopole
x_{prop}	proprotor quantity
x_p	pressure side
x_{ret}	evaluated at retarded time, τ
x_s	suction side

Superscript:

$\dot{x}$	source time derivative
x^*	optimized value
x^*	displacement thickness
x'	perturbation value
x_∞	freestream quantity
$\bar{x}$	generalized function

Symbol:

$\square^2$	wave operator, $1/c_\infty^2 \partial^2/\partial t^2 - \partial^2/\partial x_i^2$

INTRODUCTION

The potential proliferation of advanced air mobility (AAM) vehicles has led to an opportunity for aeroacoustics to be in-

Presented at the Vertical Flight Society's 79^{th} Annual Forum & Technology Display, Palm Bay, FL, USA, May 16-18, 2023. *Corresponding author: **leonard.v.lopes@nasa.gov.**

cluded in the design cycle rather than a post-design correction. AAM vehicles range in size from small unmanned aerial systems (sUAS) to larger, 6-passenger urban air mobility (UAM) vehicles, and have missions that require operation in close proximity to population who will be impacted acoustically. The acoustic impact is typically measured in some value that includes a measure of perception, such as frequency weighting. Regardless of size, AAM vehicle design must include an approximation of community impact during typical missions in order to gain acceptance and widespread use. Therefore, a design methodology is required where engineers can modify design properties to maximize aerodynamic efficiency while reducing community impact.

The computational tools required to perform design optimization for AAM vehicles during typical missions must be accurate. However, in addition to being accurate, the computational tools must also be fast due to the number of analysis executions required during design cycles. Therefore, emphasis is placed on empirical models and reduced order methods that model as much as possible and capture trends but sacrifice accuracy and flexibility. While full vehicle simulations that include realistic objective functions and noise physics are the ultimate goal of design optimization, current toolsets must focus on component-based optimization to build up and validate the simulations before being applied to full vehicles.

Propeller design optimization has been applied to propellers for decades, with computational design optimization dating back to the mid 1980s (Ref. 1). Over the past few years, focus on AAM vehicles has progressed on many fronts with limited design variables, limited noise physics in the computational models, and limited perception constraints that do not capture true community acceptance or emphasize broadband noise (Refs. 2–5). Recently, there has been effort to compute blade shape sensitivities to an acoustic metric for wing tip-mounted proprotors; however, these sensitivites have yet to be included in a design cycle (Ref. 6).

Recently, NASA has coupled the multidisciplinary design optimization framework OpenMDAO (Ref. 7), sparse nonlinear optimizer SNOPT (Ref. 8), the blade element momentum theory tool CCBlade.jl (Ref. 9) and the second generation Aircraft NOise Prediction Program ANOPP2 (Refs. 10, 11) to perform an acoustically driven design optimization for a proprotor in forward flight (Ref. 12). In a similar effort (Ref. 13), CCBlade.jl was coupled to AcousticAnalogies.jl, an implementation of the compact form (Ref. 14) of Farassat's formulation 1A (Refs. 15–17), and applied to a two-foot diameter helically twisted proprotor, denoted C24ND. The C24ND design included a constant 1.5-inch chord and twist distribution, ϕ, defined by Eq. 1, where r/R is the nondimensional radial location, P is the propeller pitch of 16 inches, D is the rotor diameter, and subscript k denotes radial station. The optimization effort resulted in a blade design called the Computationally Optimized PropRotor (COPR-3) where 3 denotes blade count.

$$\phi_k = \text{TAN}^{-1}\left(\frac{P}{\pi D}\frac{R}{r_k}\right) \tag{1}$$

Both the C24ND and the COPR-3 proprotors were fabricated and placed in the NASA Low Speed Aeroacoustic Wind Tunnel (LSAWT) at the NASA Langley Research Center, shown in Fig. 1. The experimental campaign set out to validate the design optimization process with performance and acoustic measurements. The results of this experiment showed good agreement with predictions (Ref. 18). Although the study included only tonal noise, the optimization showed that by increasing inboard chord length, decreasing tip chord length, increasing the blade pitch, and decreasing rotation rotation rate, a significant noise reduction could be achieved while simultaneously maximizing performance. Figure 2 shows the one-third octave sound pressure level (SPL) spectrum from the baseline C24ND design and from the efficiency-optimized designs, with (COPR-3) and without an overall SPL (OASPL) perception constraint.

(a) C24ND placed in NASA's LSAWT.

(b) COPR-3 placed in NASA's LSAWT.

Figure 1: Baseline C24ND and optimized COPR-3 proprotors.[Source: NASA]

The computational optimization effort that resulted in the COPR-3 design included no installation effects, one axis-aligned forward flight velocity, only tonal noise, one in-plane observer location, and a perception constraint metric that did not include the influence of human perception or community impact. While the previous effort demonstrates the feasibility of low-fidelity design optimization of UAM proprotors, UAM

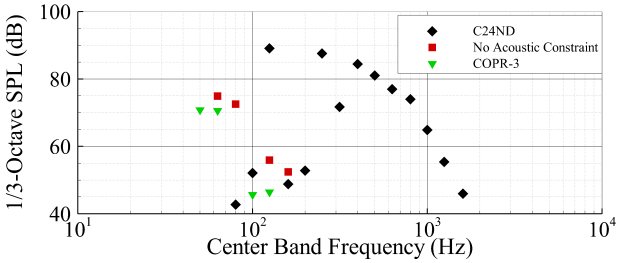

Figure 2: Computed tonal one-third octave SPL from C24ND, efficiency optimized without perception constraint, and COPR-3 proprotors.

vehicles typically have significant broadband content, operate near communities where multiple observers may be impacted, and include designs where proprotors operate near the airframe and may be impacted aerodynamically (Refs. 19–21).

This paper will explore the impact of including broadband noise prediction, an out-of-plane observer location, and an acoustic constraint that includes human impact in design optimization on the blade shape design.

BASELINE PROPROTOR DESIGN

NASA has invested much effort into addressing the acceptability of UAM vehicles. For example, the NASA Revolutionary Vertical Lift Technology (RVLT) project is investigating several UAM vehicle designs in an attempt to develop tools applicable across a wide range of applications (Ref. 22). Similarly, the NASA Transformational Tools and Technology (TTT) project is collaborating with the Georgia Institute of Technology to initiate the Research Aircraft for eVTOL Enabling techNologies (RAVEN) activity (Ref. 23). The goal of RAVEN is to design, develop, and flight test a 1,000 lb gross-weight-class eVTOL research aircraft and to disseminate the aircraft geometry and test data to support the research community. The aircraft is being designed to use commercial-off-the-shelf (COTS) components to the maximum extent practicable to save costs and to accelerate the development schedule; however, since the goal of RAVEN is to disseminate geometry, the effort offers the ability to design proprotors that may be ultimately fabricated in an attempt to reduce noise.

While the goal of the optimization process is to include as much realism as possible, for instance multiple proprotors similar to the work done by Zawodny et al. (Ref. 24), the baseline design for this current work will include only an isolated proprotor and of the scale to be fabricated and placed in the NASA LSAWT. Also, in the spirit of dissemination, the baseline design, while not a particularly realistic proprotor, must be a design that is simple to describe (Ref. 18). The C24ND propeller shown in Fig. 1a is a 3:1 scale, three-bladed helically twisted propeller with a constant spanwise chord distribution (c = const.), as well as a nominally spanwise-constant NACA 0012 airfoil profile. The helical twist distribution is defined as in Eq. 1. The primary geometric properties of the C24ND propeller are provided in Table 1.

Table 1: Geometric properties for the C24ND propeller.

Parameter	Value
c, in. (mm)	1.5 (38.1)
P, in. (mm)	16.0 (406.4)
D, in. (mm)	24.0 (609.6)

COMPUTATIONAL DESIGN OPTIMIZATION PROCESS

The computational design optimization process involves four computational blocks: aerodynamic, source noise, perception constraint, and a nonlinear optimization. These four computational blocks are coupled within the OpenMDAO framework (Ref. 7). OpenMDAO is an open-source Python implementation of the modular analysis and unified derivatives (MAUD) (Ref. 25) approach to multidisciplinary design, analysis, and optimization (MDAO). OpenMDAO allows the application developer to express an analysis as a connected series of components, where each component uses inputs to calculate not only the outputs, but also the derivatives of the outputs with respect to the inputs. It then assembles these partial derivatives together into a total derivative, i.e., the derivative of the problem objective and constraints with respect to the design variables. The OpenMDAO framework is used here to couple together the aerodynamics, source noise predictions, perception constraints, and an optimizer package called pyOptSparse which is used to call SNOPT, a sparse nonlinear optimizer (Ref. 8).

A simplified extended design structure matrix (XDSM) (Ref. 26) showing the relationship between the computational blocks is shown in Fig. 3. The k subscripts indicate a variable that varies along the blade radial station and the $*$ superscripts indicate the final optimized values returned by the optimizer. The aerodynamic calculation takes information describing the shape and motion of the propeller and calculates aerodynamic performance metrics such as thrust and efficiency. It also returns $\boldsymbol{y}_k$, the blade element locations in the same coordinate system, and $\boldsymbol{F}_k$, the spanwise propeller loading generated by each blade element. The source noise computational block takes in the source information from the aerodynamic calculation and other parameters, such as observer location $\boldsymbol{x}$, and returns acoustic metrics predicted at that observer location such as the acoustic pressure time history (APTH) and/or the one-third octave proportional band SPL spectrum (PBS). The final computational block takes in the acoustic metrics at the observer locations and computes a final perception constraint value that is provided to the optimizer.

At the start of the design process, the thrust, efficiency, and acoustic constraint of the C24ND are predicted. This is shown as the black diamond symbols in Fig. 4, which shows the efficiency and RPM, and in Fig. 5, which shows the blade properties. Afterward, the proprotor is optimized to provide the best possible efficiency while maintaining a thrust constraint set to the value of the C24ND thrust. This is shown as red square symbols in Figs. 4 and 5 and is denoted as 'no acoustic constraint'. Then several more optimizations are

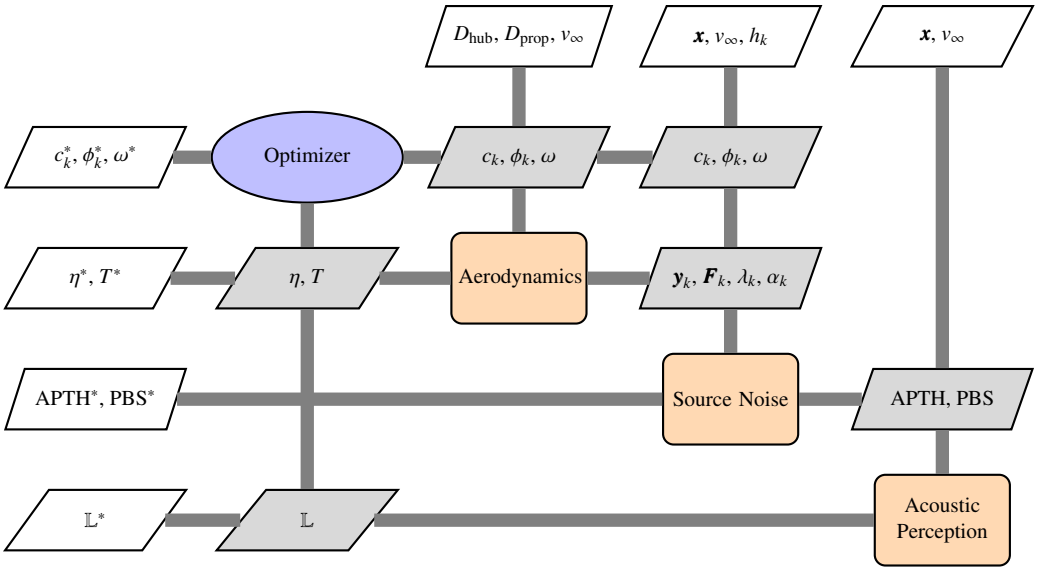

Figure 3: Extended design structure matrix (XDSM) for proprotor design optimization.

performed with an ever more restrictive acoustic constraint, in 0.1 dB or dBA increments, while maintaining the same thrust constraint. This starts with the acoustic constraint value calculated from the 'no acoustic constraint' optimization until either the optimizer has difficulty providing a design that achieves both the required thrust and acoustic constraints or an efficiency of 0.81 is reached. This defines a Pareto front that couples efficiency to the acoustic constraint and is shown as a blue line in Figs. 4 and 5. After the Pareto front is defined, the acoustic constraint that results in an efficiency of 0.83 is used to define a 'target efficiency' design that allows the comparison of blade designs using differing acoustic constraints. This is denoted as green gradient symbols in Figs. 4 and 5.

A summary of the design optimization is the following:

- Objective:
  - Maximize efficiency, η
- Design Variables:
  - $c(r)$, chord distribution at six spline control points
  - $\phi(r)$, twist distribution at six spline control points
  - ω, proprotor rotation speed
- Constraints:
  - T, thrust at cruise
  - $\mathbb{L}$, acoustic perception metric

Each of the computational blocks shown in Fig. 3 is explained further in the following sections.

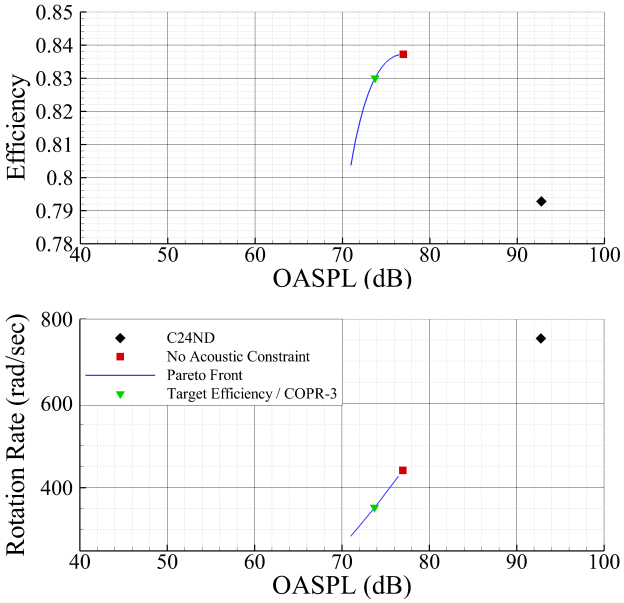

Figure 4: Efficiency and RPM during proprotor design process of COPR-3.

Aerodynamics

The propeller aerodynamics are predicted here using blade element momentum theory (BEMT) implemented in CCBlade.jl (Ref. 9). BEMT begins by dividing the blade span into a finite number of radial stations, or "blade elements" (Ref. 27). Each blade element is treated as an independent airfoil with associated lift and drag curves defined in a C81 table. A control volume is then formed that encloses the propeller and the flow far upstream and downstream. By applying a momentum balance to this control volume and including the interaction between the fluid and blade elements, the velocity induced by the propeller in the axial and circum-

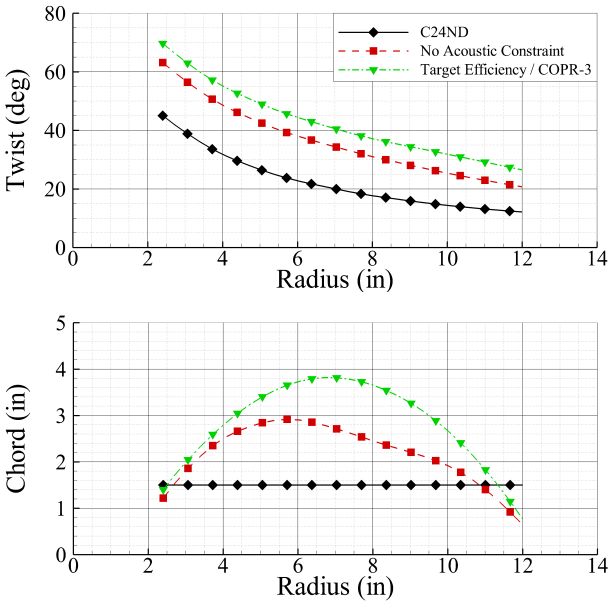

Figure 5: Twist and chord blade properties during proprotor design process of COPR-3.

ferential directions can be predicted. The induced velocities can then be used to calculate desired propeller performance metrics, such as the necessary input power, net torque and thrust, and propeller efficiency.

While not as capable as more sophisticated vortex-based methods (Ref. 28) or computational fluid dynamics (CFD) (Refs. 11, 29), BEMT works quite well for isolated proprotors experiencing on-axis flow, and the computational efficiency of BEMT makes it especially attractive for preliminary design work (e.g., where a large number of designs are to be evaluated quickly), and highly multidisciplinary design optimizations (e.g., where the propeller aerodynamics are one small piece of a large computational model).

BEMT assumes that there is no interaction between radial stations, and is thus not suitable for blades with significant spanwise flow. The propeller blades considered in this work are unswept and rather slender, making BEMT an appropriate choice. The particular form of BEMT currently implemented in CCBlade.jl assumes steady, level flight with the propeller shaft axis aligned with the incoming flow. This implies that the loads predicted by CCBlade.jl will be steady, i.e., they will not be a function of azimuthal position or time. Fortunately, steady propeller noise sources are expected to be the most significant tonal source for the configuration considered in this work (Ref. 30).

Source Noise

UAM vehicles generate many noise sources that contribute to the overall noise signature. These include tonal noise sources, such as periodic blade loading, blade-vortex interaction (BVI), and electric motor noise, and broadband noise sources, such as broadband self-noise, turbulent ingestion noise (TIN), blade-wake interaction (BWI), and rotor-wake interaction (RWI). While all noise sources are important for full vehicle noise prediction, this study will consist of the two noise components most important for a single proprotor design: tonal noise and broadband self-noise.

The tonal noise content will be calculated by way of Farassat's Formulation 1A (F1A) (Refs. 15–17), implemented in ANOPP2 (Ref. 10) as the ANOPP2 Farassat Formulations Internal Functional Module (AFFIFM) (Ref. 31), which uses generalized function theory (Ref. 32) and Lighthill's stress tensor (Refs. 33, 34) to define the acoustic pressure generated by a noise-generating mechanism. F1A is derived by applying a free-space Green's function to the Ffowcs Williams and Hawkings (FWH) equation (Ref. 35), Eq. 2, which includes two surface source terms and one volume source term. The surface terms are identified by the Dirac delta function, $\delta(f)$, and the volume term is identified by the Heaviside function, $H(f)$, where f is the time-dependent FWH surface. The surface f can be impermeable, such as a rotor blade surface, or permeable, such as a computational surface surrounding the entire rotorcraft. In Eq 2, Q, $\boldsymbol{L}_i$, and $\boldsymbol{T}_{ij}$ are the monopole, dipole, and quadrupole source terms, respectively, and are functions of the local flow properties and kinematics of the surface. In typical low-speed applications such as UAM proprotors, the quadrupole term may be safely ignored.

$$\bar{\Box}^2 p' = \frac{\partial}{\partial t}[Q\delta(f)] - \frac{\partial}{\partial \boldsymbol{x}}[\boldsymbol{L}\delta(f)] + \frac{\bar{\partial}^2}{\partial \boldsymbol{x}\partial \boldsymbol{x}}[\boldsymbol{T}H(f)] \qquad (2)$$

For reasons stated above, computational time is a strong driver in computational method selection due to the number of cycles required for design optimization. The compact assumption applied to F1A can potentially reduce the costly evaluation of a surface integral into a very efficient evaluation of a line integral. Achieving the compact form of F1A requires two assumptions: 1) the observer position is very far away with respect to the characteristic size of the surface, typically the chord length, and 2) the time it takes the noise to propagate across the surface is much larger than the typical period of surface pressure fluctuations. Both of these assumptions are valid in this application. In this case, the surface integral can be replaced by a line integral along the spanwise direction, and, if ignoring surface deformation, can reduce F1A to its simplified compact form. This form includes a monopole term, shown in Eq. 3, and a dipole term, shown in Eq. 4, where the definition of the radiation coefficients, $\mathscr{C}_{1A}$, $\mathscr{D}_{1A}$, and $\mathscr{E}_{1A}$ can be found in Reference 14.

$$\frac{4\pi}{\rho_\infty} p'_m(\boldsymbol{x},t) = \int_{F=0} \left[\Psi \mathscr{C}_{1A} K\right]_{\text{ret}} \mathrm{d}u \qquad (3)$$

$$4\pi c_\infty p'_d(\boldsymbol{x},t) = \int_{F=0} \left[\dot{\boldsymbol{F}} \mathscr{D}_{1A} K\right]_{\text{ret}} \mathrm{d}u + \int_{F=0} \left[\boldsymbol{F} \mathscr{E}_{1A} K\right]_{\text{ret}} \mathrm{d}u \qquad (4)$$

The second noise source included in this study is caused by the self-generated broadband turbulent boundary layer interacting with the proprotor's trailing edge causing self-generated noise, also known as 'broadband self-noise'. The

broadband self-noise content will be calculated by leveraging a semiempirical prediction methodology developed by Brooks et al. (Ref. 36) who derived relationships between airfoil Mach number, Reynolds number, and angle of attack to boundary layer properties and, subsequently, boundary layer properties to noise. This methodology was placed in a rotating frame for the prediction of broadband self-noise for helicopter main rotors (Refs. 37,38). The methodology described in References 37 and 38, excluding the broadband wake interaction, has been implemented in ANOPP2 (Ref. 10) as the ANOPP2 Self-Noise Internal Functional Module (ASNIFM), which can be executed by a command line interface called the ANOPP2 Broadband Acoustic Rotor Tool (ABART). Recently, ABART was applied to UAM propellers to some success (Refs. 39,40).

Broadband self-noise consists of five source noise mechanisms shown in Fig. 6, taken from Brooks et al. (Ref. 36): turbulent boundary layer trailing edge (TBLTE), laminar boundary layer vortex shedding (LBLVS), trailing edge separation/stall, bluntness vortex shedding (BVS), and tip vortex formation. Broadband self-noise is significantly influenced by surface roughness and, therefore, by the fabrication material of the blade surfaces or trip configuration. In the current work, we will be focusing on computational trip settings to simulate a surface material like the isolated propeller test performed previously (Ref. 18). This material emphasizes TBLTE noise while suppressing LBLVS noise due to the surface roughness that acts like a boundary layer trip.

There were three challenges encountered during the implementation and execution of ASNIFM for this design optimization. The first challenge was selecting a series of empirical constants used in the broadband self-noise prediction that were applicable across all designs. Achieving the closest predictions against measurements from Reference 18 required selecting a trip setting of 0.5, which amounts to using an average of the untripped and fully tripped NACA 0012 airfoil, taken from Brooks et al. (Ref. 36). The second challenge was the baseline design's high rotation rate, which resulted in tip speeds that were well outside the bounds of the airfoil data collected by Brooks et al. This caused broadband noise calculations of higher RPM designs to be underpredicted; however, the trends (and therefore the designs) were acceptable and led to appropriate, lower-RPM designs where the predictions were more in line with measurements. Comparisons between predictions and measurements of C24ND and COPR-3 proprotors for several tip Mach numbers and advance ratios will be published shortly after this work (Ref. 41). The third challenge was that bluntness noise may vary with angle of attack; this was not investigated by Brooks et al. and, therefore, is not included in the BPM empirical method upon which ASNIFM is built. NASA is studying and improving the bluntness noise model and an updated model will be included when it becomes available (Ref. 41). Furthermore, using the Brooks model for bluntness noise required empirical constants that had to be calibrated depending on the design conditions. This could not happen during successive iterations with an ever-limiting acoustic constraint. As a result, the current optimization effort does not include the bluntness noise mechanic.

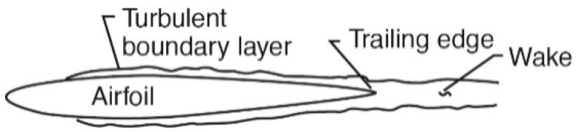

(a) Turbulent bondary layer trailing edge (TBLTE)

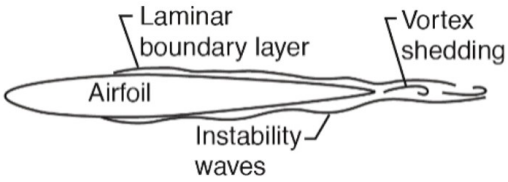

(b) Laminar boundary layer vortex shedding (LBLVS)

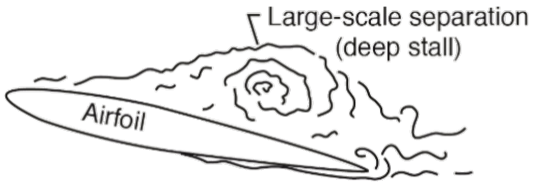

(c) Trailing edge separation/stall

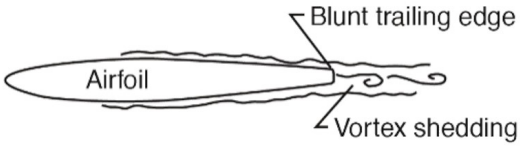

(d) Bluntness vortex shedding (BVS)

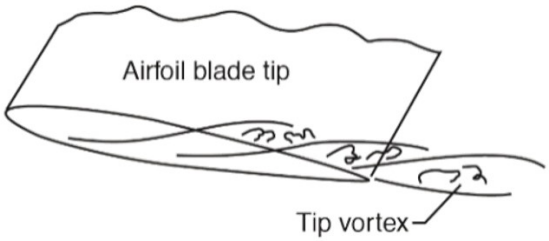

(e) Tip vortex formation

Figure 6: Flow conditions producing airfoil blade self-noise (Ref. 36).

The result of AFFIFM is a time history of acoustic pressure (APTH) and that of ASNIFM is a one-third octave PBS that can be provided to the perception constraint portion of the design optimization. In addition to the APTH for tonal noise and PBS for broadband self-noise, AFFIFM and ASNIFM can also provide the derivatives of those quantities with respect to the inputs provided via backward differentiation, in a similar manner as CCBlade.jl.

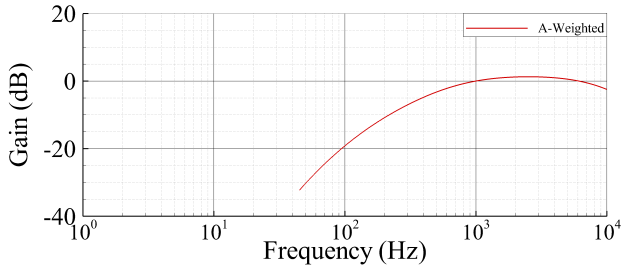

Figure 7: A-weighting functions.

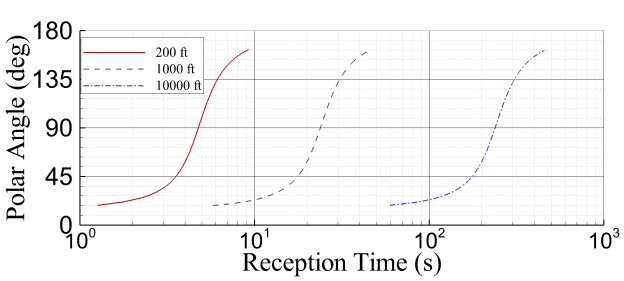

Figure 8: Polar directivity of level flyover events at notional velocity.

Acoustic Perception

Once the APTH for tonal noise and PBS for broadband self-noise are determined by the source noise block of the optimization computation, a perception constraint value is calculated in the constraint computational block of the design optimization. There are several different potential perception constraints that may be calculated from the same source noise input. These include total acoustic energy computations, such as OASPL like that used previously in Ref. 12. This is adequate for tonal noise, which contains a small number of closely grouped, low-frequency tones; however, in the current work, broadband noise will be studied, which includes, by definition, a broad range of frequencies including high frequencies that are perceived as more impactful by a human. In the current work, the ANOPP2 Acoustic Analysis Utility (AAAU) will be leveraged to include techniques that account for human perception. A common technique is the A-weighting attenuation curve, shown in Fig. 7, which emphasizes noise at frequencies heard more efficiently by a human and suppresses noise at those not as efficiently heard by a human. The C24ND was designed as a scale-model representation of a UAM proprotor; however, A-weighting requires full-scale frequencies. In this study, for the purpose of A-weighting, all noise results are scaled to a 6-ft diameter proprotor similar to that being designed for the RAVEN vehicle mentioned previously. The AAAU is also capable of providing derivatives to derived quantities, such as A-weighted OASPL, with respect to the inputs quantities, such as APTH and/or PBS.

In the previous work (Ref. 12), only one observer position in the plane of the proprotor was used in the computation that resulted in the COPR-3 design. Since the previous work focused on tonal noise only, which is primarily an in-plane noise source for these types of flight conditions, an in-plane observer position was adequate. In the current work, broadband noise sources will be included in the acoustic constraint, which are primarily out-of-plane noise sources. Additionally, the ultimate goal of design optimization is to reduce human perception of a UAM flight event. Figure 8 shows the polar directivity of the noise emission toward an observer on the ground, where 0° is the nose of the aircraft and 180° is the tail, for three vehicle altitudes all traveling at the same velocity. Assuming the proprotor is in a vehicle thrust orientation, where the rotation axis is aligned with the flight direction, a polar angle of 90° is where the proprotor is oriented such that the observer is in the plane of the proprotor. The range of reception time shown in Fig. 8 at this angle is shorter compared to when the observer is behind the proprotor, where the polar emission angle is 135°. However, a polar angle of 90° is where the vehicle is closest to the observer. Therefore, for community impact, both in-plane and out-of-plane observer positions must be studied. In the current work, an in-plane observer (11.6 proprotor radii away) and an observer oriented behind the rotor (16.4 proprotor radii at 135°) will be studied separately. These correspond to microphone locations in the LSAWT during the previous design optimization effort. However, note that the ultimate goal is to define an acoustic constraint metric that includes the entire directivity for a realistic flight event. This type of acoustic constraint will require several evaluations of source noise per acoustic constraint evaluation and will be a challenge to execute in a design optimization where many (thousands) of evaluations are required. This will be the goal of follow-on work.

DESIGN PROPERTY SWEEPS

The evaluation of efficiency and acoustic constraints are calculated for a large number of designs during the design optimization calculation, starting with the baseline C24ND and ending with an optimized design that sacrifices efficiency for a reduction in the acoustic constraint. An important characteristic of the efficiency and acoustic constraints is their behavior as related to various design properties. Before a design optimization occurs, a study including sweeps of design properties can show potential local minima in efficiency and/or the acoustic constraint that may give the optimizer problems resulting in a failed design optimization. Three sweeps of design properties were performed, holding one of the three design properties constant and varying the other two. The baseline design of the design property sweeps is the C24ND design with the exception of collective, which was increased by 10°. This was chosen because during the design optimization shown in the following section, the optimization quickly sacrifices RPM for an increase in collective and the increase in collective centers the sweep on design properties more closely in line with those ultimately reached by the design optimization. In addition, the chord was increased uniformly in order to simplify the parameter sweep. This is not the case in the design optimization that will be presented in the next section.

Figure 9 shows the proprotor efficiency under many combinations of RPM, uniform chord length, and proprotor collec-

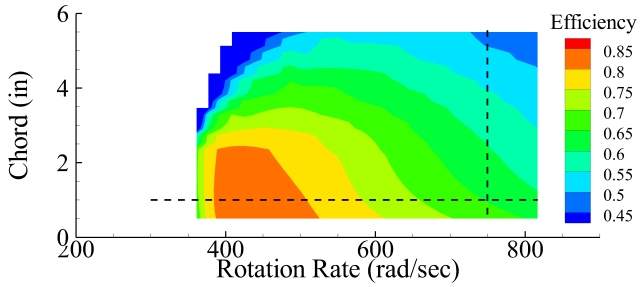

(a) RPM and chord length design property sweeps of efficiency.

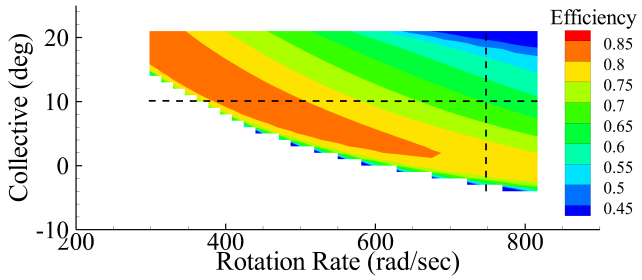

(b) RPM and collective design property sweeps of efficiency.

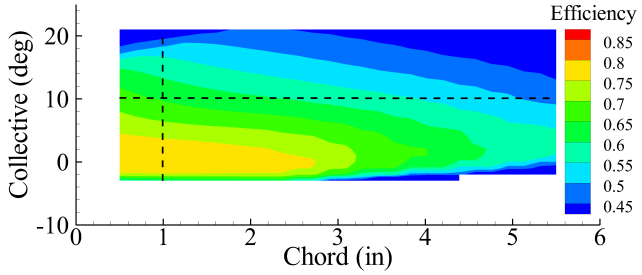

(c) Chord length and collective design property sweeps of efficiency.

Figure 9: Design property sweeps of chord length, collective, and RPM of proprotor efficiency.

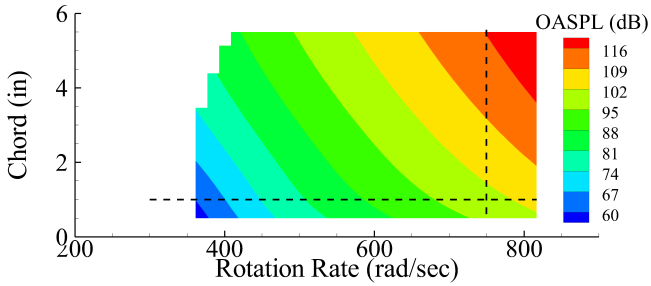

(a) RPM and chord length design property sweeps of OASPL.

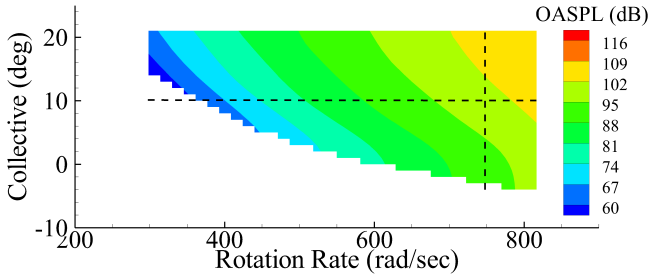

(b) RPM and collective design property sweeps of OASPL.

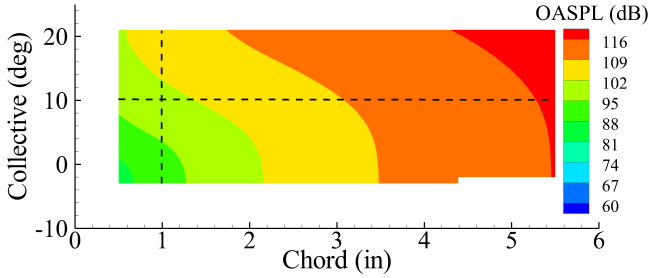

(c) Chord length and collective design property sweeps of OASPL.

Figure 10: Design property sweeps of chord length, collective, and RPM of total noise, unweighted, in-plane OASPL.

tive angle. Dashed lines indicate the intersection of the three-dimensional design property sweeps for comparison. The combinations of design properties that resulted in negative thrust are excluded from the figures. In general, the efficiency is well-behaved under many combinations of the design properties. One exception is at high values of chord shown in Fig. 9a where the airfoil database upon which CCBlade.jl relies may be malformed. These combinations of chord, twist, and RPM are encountered during the design optimization and did cause some computational difficulties; however, the design optimization was able to get through this region unaffected. These airfoil tables will be improved in future iterations of proprotor design optimization.

Figure 10 shows the total unweighted OASPL predicted in the plane of the rotor calculated during the design property sweeps. The breakdown of tonal and broadband noise is not shown because the entire sweeps are dominated by tonal noise. As expected, as the chord length at the tip or the tip speed, via RPM, are increased, the in-plane noise increases significantly. In addition, the collective angle only has a small influence on noise due to the dominance of the tonal noise source, which is a strong function of the blade volume and speed at the tip. Overall the design properties sweep is very smooth, resulting in well-behaved functions ideal for design optimization.

Figures 11 and 12 show the tonal and broadband noise, respectively, for an A-weighted OASPL at the out-of-plane observer position. Similar to the previous study, all curves are relatively smooth and well behaved, numerically, which will result in an overall well behaved design optimization. Several characteristics of the acoustic constraint can be seen in these figures. The first is that tonal noise is significantly reduced and is, in general, on the order of the broadband noise. This was not the case for the unweighted OASPL in the plane of the proprotor. While some of the noise reduction can be attributed to the observer being further away, the overwhelming majority is due to the thickness noise directivity pattern, which is significantly reduced out of the proprotor plane. Also, while the loading noise has increased significantly, it did not increase at a commensurate rate to overcome the reduction in thickness

noise. The second characteristic is that the tonal noise is lower than the broadband noise at lower RPM values, which was the primary driver to noise reduction in the previous optimization study conducted in the plane of the proprotor. This can clearly be seen in design property sweeps of constant collective in Figs. 11a and 12a and constant chord in Figs. 11b and 12b. The third characteristic is the effect of collective on broadband noise at higher chord values in Fig. 12c. A higher collective and larger chord length would result in a larger boundary layer and a shift in broadband noise from higher frequency to a freqeuncy range more impacted by A-weighting. However, even though the frequency weighting did increase the broadband noise impact in the shifted frequency, the BPM model also includes a reduction in noise amplitude. The fourth characteristic to note is that the broadband noise is the dominant noise source at high collective and small chord length designs, shown in Fig. 12c, but tonal noise is dominant at low collective and large chord length designs, shown in Fig. 11c. Since, ultimately, the design properties will include many combinations of twist and chord, this suggests that different parts of the blade may include different dominant noise sources. This will have to be investigated further in a follow-on effort.

Figure 13 shows the total, A-weighted OASPL at an observer location out of the proprotor plane. As expected, the total noise is a sum of tonal and broadband and has characteristics of either tonal or broadband components depending on which is the dominant noise source. In all three design property sweeps, neither tonal nor broadband noise is the overall dominant noise source. Surprisingly, the collective and chord sweeps show the least amount of variation in the noise level. This is surprising due to the nature of the tonal noise where an increase in chord at the tip is a strong driver of noise.

These proprotor design property sweeps suggest two important characteristics that will be encountered during the design optimization. The first is that both tonal and broadband noise are expected to be important and neither can be ignored. The second is that all three design properties have a strong influence on the noise with, not surprisingly, RPM having the strongest influence. In the next section, results from the design optimization for in the rotor plane and out of the rotor plane, with and without A-weighting, will be shown. This analysis includes a spectral analysis of each noise component.

DESIGN OPTIMIZATIONS

Design optimizations were performed for combinations of source noise, frequency weighting, and observer position. Figure 14 shows the efficiency and RPM for tonal noise only, broadband noise only, and total noise using no frequency weighting and an in-plane observer position. As expected, tonal noise is the dominant factor and the blade shape result of the total noise optimization is identical to the tonal noise only blade shape shown in Fig. 5 where tonal noise is indistinguishable from total noise. The blade shape is shown in Fig. 15 for the unweighted, in-plane observer calculation including the C24ND, no acoustic constraint, and for an acoustic constraint that included tonal noise only, broadband noise

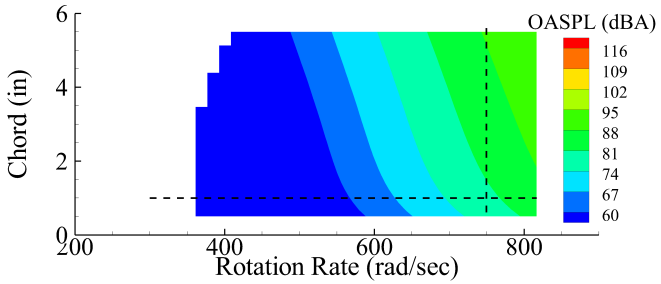

(a) RPM and chord length design property sweeps of tonal OASPL.

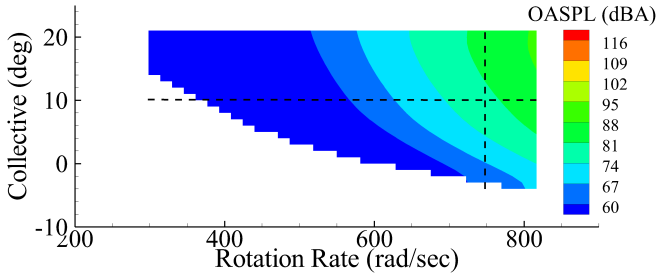

(b) RPM and collective design property sweeps of tonal OASPL.

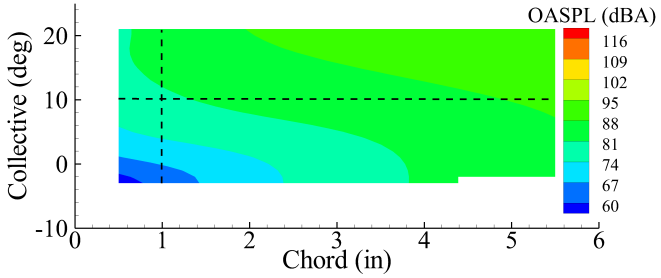

(c) Chord length and collective design property sweeps of tonal OASPL.

Figure 11: Design property sweeps of chord length, collective, and RPM of tonal noise only, A-weighted, out-of-plane OASPL.

only, and total noise. Although it does not affect the blade shape design result of the optimization, the broadband noise only optimization does sacrifice blade twist for an increase in chord length.

Figure 16 shows the unweighted one-third octave SPL spectrum for the tonal noise only, broadband noise only, and total noise at the in-plane observer position for the C24ND, design without an acoustic constraint, and target efficiency of 0.83. Figure 16a show the tonal noise only predictions. The predictions for the C24ND have significant higher harmonic content and the optimized designs achieved significant noise reduction by first reducing that harmonic content. This is primarily due to the reduction of volume at the tip of the proprotor being compensated by an increasing volume inboard and moving the loading inboard; while good for performance, this also significantly reduces noise. This is shown in Fig. 17, which shows the thickness and loading breakdown for the C24ND, no acoustic constraint, and target effieincy designs at model-

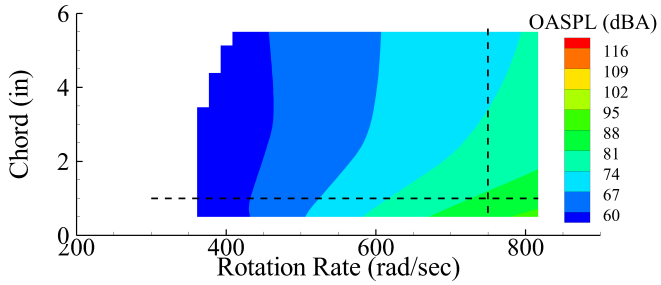

(a) RPM and chord length design property sweeps of broadband OASPL.

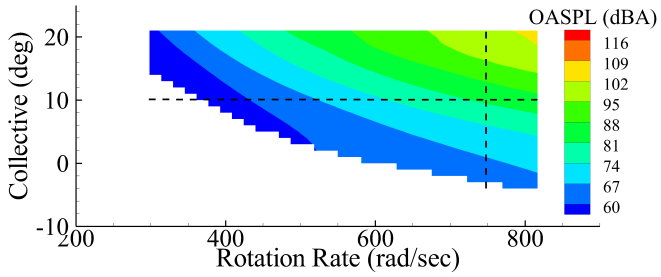

(b) RPM and collective design property sweeps of broadband OASPL.

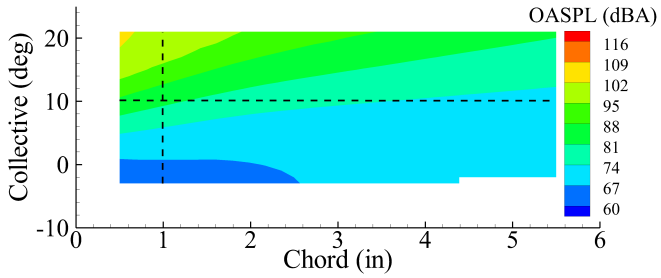

(c) Chord length and collective design property sweeps of broadband OASPL.

Figure 12: Design property sweeps of chord length, collective, and RPM of broadband noise only, A-weighted, out-of-plane OASPL.

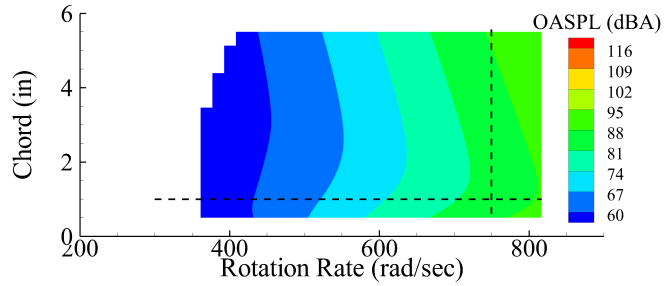

(a) RPM and chord length design property sweeps of total OASPL.

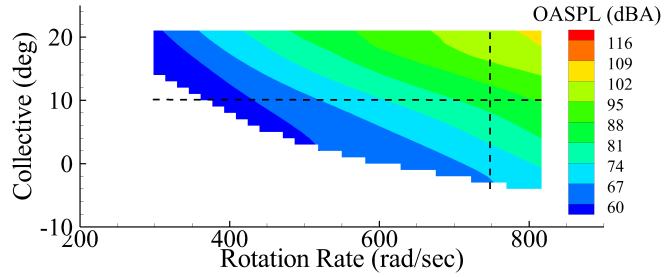

(b) RPM and collective design property sweeps of total OASPL.

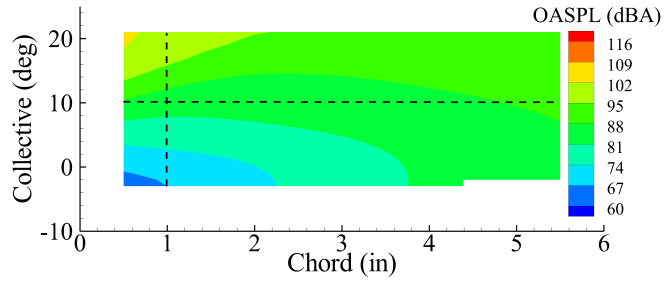

(c) Chord length and collective design property sweeps of total OASPL.

Figure 13: Design property sweeps of chord length, collective, and RPM of total, A-weighted, out-of-plane OASPL.

scale frequencies. Interestingly, the C24ND is thickness noise dominant but the no acoustic constraint design is loading noise dominant. Figure 16b shows the broadband noise only predictions. The broadband noise is evident above 500 Hz and is reduced as a result of the optimization; however, this is due to the tonal noise driving the design optimization, not because the design optimization invested in broadband noise reduction specifically. The peak in the broadband noise is shifted to lower frequencies and the amplitude is attenuated. This is due to the increase in chord length, resulting in a larger boundary layer and, therefore, reduced Strouhal number. Interestingly, the largest reduction in noise on a per-frequency basis came from the optimization without an acoustic constraint; limiting the acoustic constraint reduced the noise further at the expense of efficiency.

Figures 18 and 19 show the efficiency, RPM, and blade shape characteristics of the A-weighted, out-of-plane predictions for the C24ND, no acoustic constraint, and target efficiency design optimizations, respectively. Figure 18 shows that the tonal noise source is the primary noise source for the C24ND and the no acoustic constraint optimization results in significantly lower tonal noise, reducing it well below the broadband noise. This is similar to the unweighted, in-plane observer optimization. The acoustic constraint optimizations of the A-weighted, out-of-plane optimizations start by reducing both tonal and broadband noise, though broadband noise is the driving factor. As the acoustic constraint becomes more restrictive, the tonal noise falls faster than the broadband noise until the point where the broadband noise is the only driving factor of the noise optimization.

Comparing Figs. 14 and 18 demonstrates the impact of frequency weighting and directivity on the tonal and broadband noise curves. Generally, the overall level of tonal noise is significantly reduced by more than 30 dB, while the overall level of broadband noise remains unchanged. Figure 19 shows how the broadband noise reduces twist in order to increase chord at the outboard spanwise sections of the proprotor. This is due to

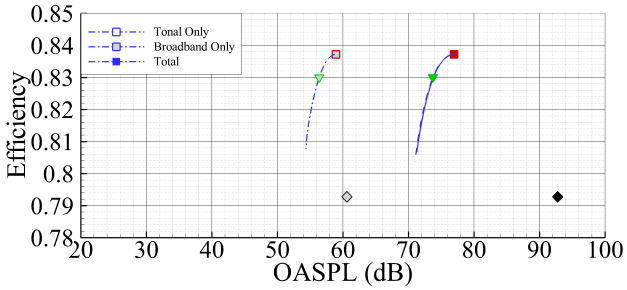

(a) Efficiency during design optimization.

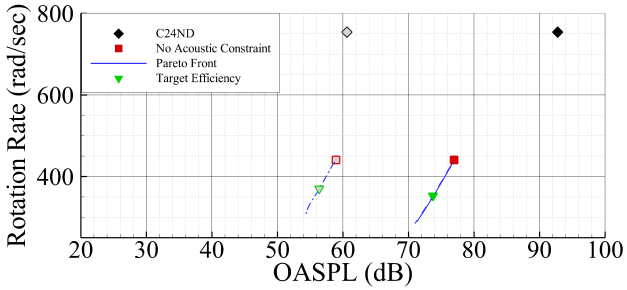

(b) RPM during design optimization.

Figure 14: Efficiency and RPM during design process of using unweighted OASPL at an observer in the plane of the proprotor as the acoustic constraint.

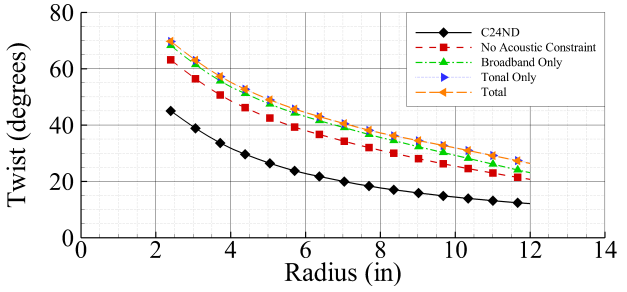

(a) Blade twist.

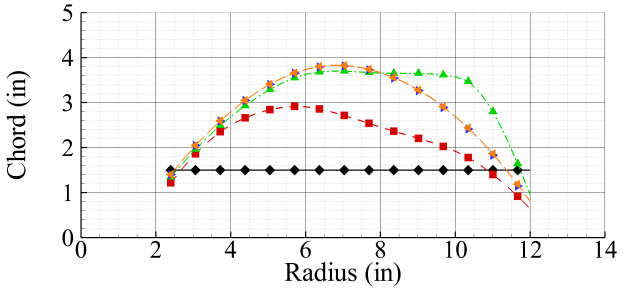

(b) Blade chord.

Figure 15: Efficiency and RPM during design process of using unweighted OASPL at an observer in the plane of the proprotor as the acoustic constraint.

the optimizations increasing chord length in order to increase boundary layer size which decreases the frequency and amplitude. This can be seen in Fig. 20, which shows the boundary layer thickness and displacement thickness for the C24ND, design without an acoustic constraint, and design with the target efficiency. The blade shape of the total noise optimization is very similar to the broadband noise only noise optimization, though some differences do exist in the chord length at the midspan of the blade.

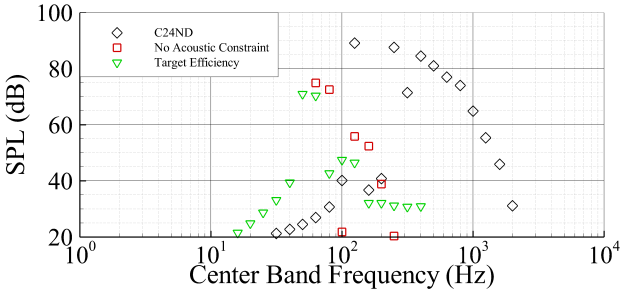

(a) Prediction of tonal noise, unweighted, in-plane tonal SPL.

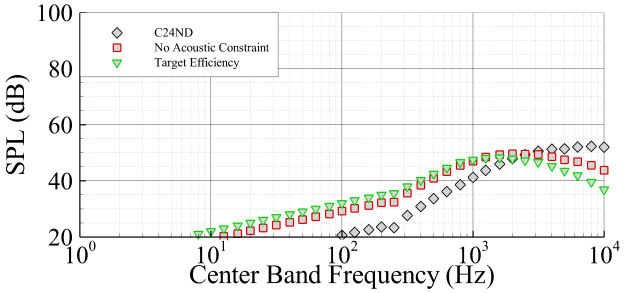

(b) Prediction of broadband noise, unweighted, in-plane briadband SPL.

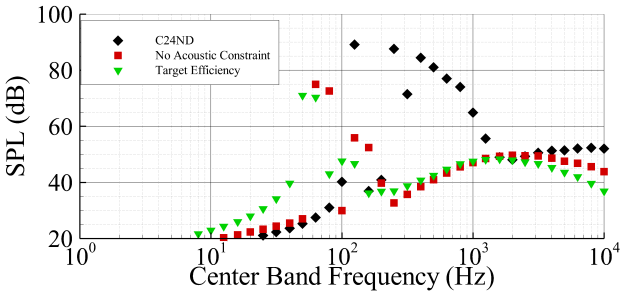

(c) Prediction of total noise, unweighted, in-plane total SPL.

Figure 16: Predictions of tonal noise only, broadband noise only, and total unweighted SPL at an observer in the proprotor plane.

Figure 21 shows the tonal noise only, broadband noise only, and total noise predictions for the C24ND, no acoustic constraint, and target efficiency for the optimization with an acoustic constraint that includes A-weighting and an out-of-plane observer position. Similar to the unweighted, in-plane observer design optimization, the tonal noise starts with a significant amount of higher harmonic content due to the volume at and speed of the tip of the proprotor. Comparing 16a and 21a shows the impact of A-weighting and observer position on the tonal noise, which is significant. Tonal predictions of the C24ND show a reduction of the peak from approximately 90 dB to 65 dBA, while for the target efficiency from approximately 70 dB to 35 dBA. Comparing 16b and 21b shows the impact of A-weighting and observer position on the

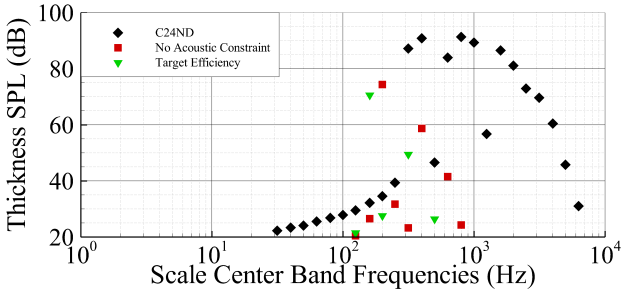

(a) Thickness noise.

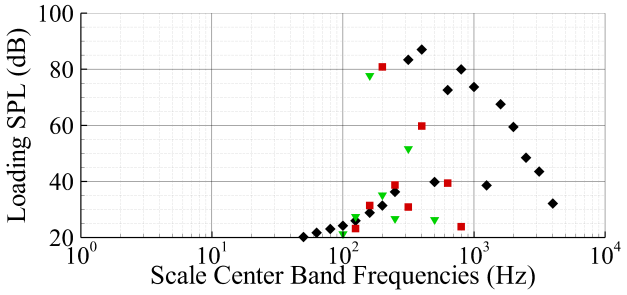

(b) Loading noise.

Figure 17: Prediction of thickness and loading noise, unweighted, at an in-plane observer position.

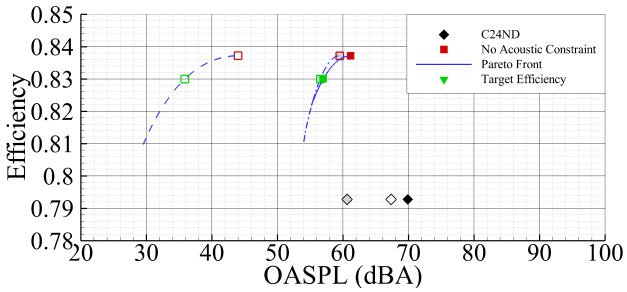

(a) Efficiency during design optimization.

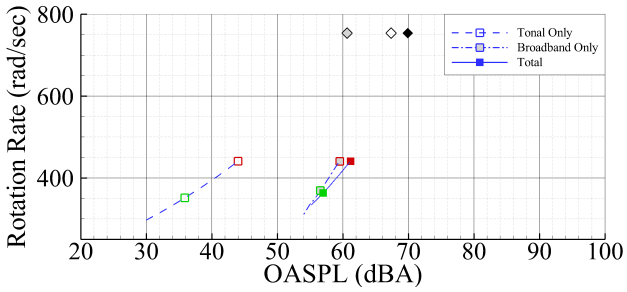

(b) RPM during design optimization.

Figure 18: Efficiency and RPM during design process of using A-weighted OASPL at an observer out of the plane of the proprotor as the acoustic constraint.

broadband noise, which is much less significant when compared to the tonal noise impact. Broadband predictions of the C24ND and the target efficiency optimization cases show that the peak remains relatively the same at 60 dB or 60 dBA, respectively. A direct comparison is difficult due to the different

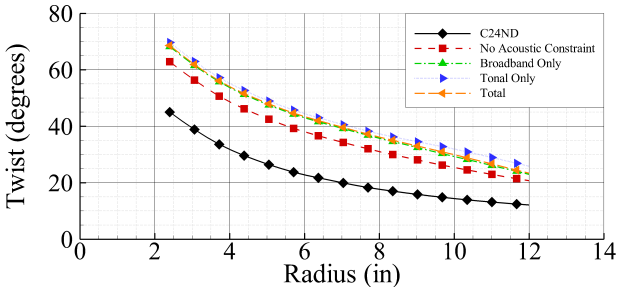

(a) Blade twist.

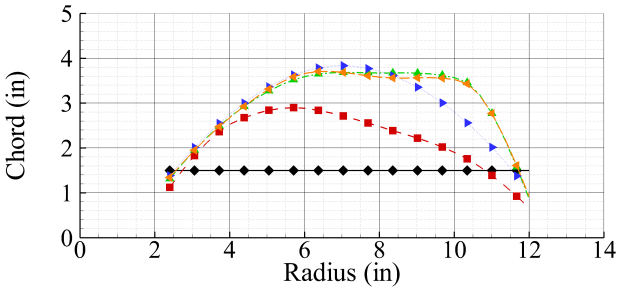

(b) Blade chord.

Figure 19: Twist and chord blade properties during proprotor design process including an acoustic constraint of A-weighted OASPL at an out-of-plane observer.

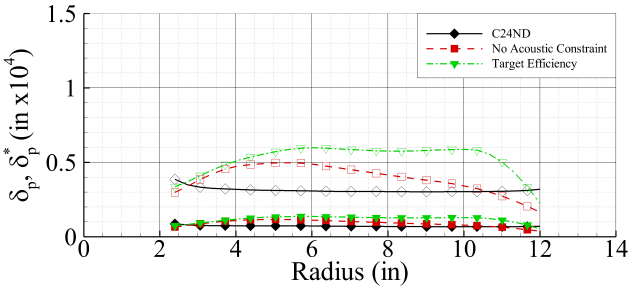

(a) Pressure side.

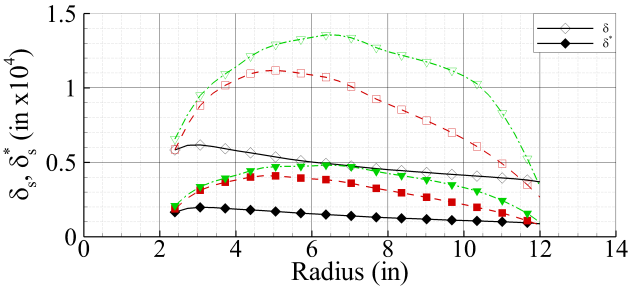

(b) Suction side.

Figure 20: Pressure and suction side boundary layer thickness and displacement thickness predictions for the C24ND, design without an acoustic constraint, and design with A-weighted OASPL at an out-of-plane observer at the target efficiency.

metrics; however, from an overall impact on the design optimization, this shows a deemphasis on the tonal noise whereas

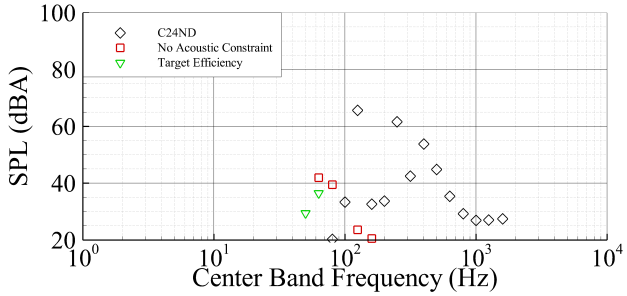

(a) Prediction of A-weighted tonal SPL.

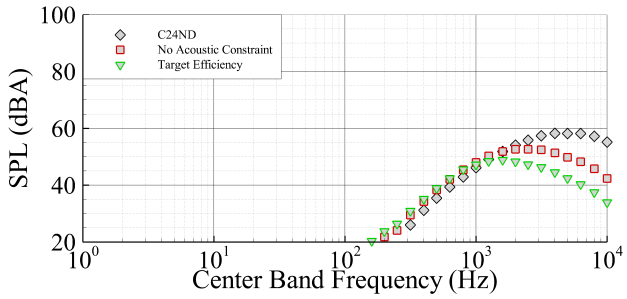

(b) Prediction of A-weighted broadband SPL.

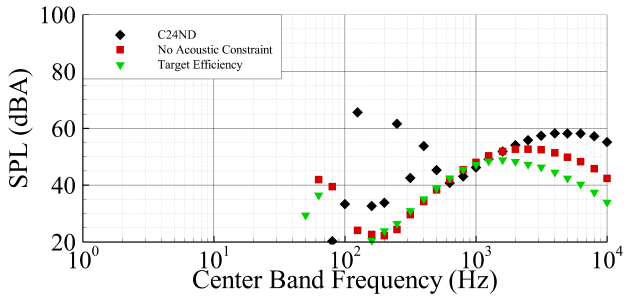

(c) Prediction of A-weighted total SPL.

Figure 21: Predictions of tonal noise only, broadband noise only, and total A-weighted SPL at an observer out of the proprotor plane.

the broadband noise remains the same. Figure 21c shows that, as expected, the tonal noise is impactful for the C24ND even with A-weighting and an out-of-plane observer position; however, the no acoustic constraint and the target efficiency designs show lower levels of tonal noise when compared to broadband noise. This, again, points to the importance of broadband noise on the out-of-plane design optimizations.

Figure 19 gives the impression that the optimizer is converging on a design with a constant chord at several radial stations of the blade; however, this is a coincidence due to the efficiency chosen for the target efficiency design. Figure 22 shows the twist and chord achieved during a series of design optimizations that define the Pareto front shown in Fig. 18. Also shown is the blade design for the target efficiency. The design optimization keeps increasing chord at outboard spanwise sections while increasing the twist along the entire blade and decreasing RPM. If a more restrictive acoustic constraint was chosen, in order to achieve a lower target efficiency, the blade design may have a larger chord outboard than inboard. The structural feasibility of that type of design is unclear, and motivated the particular target efficiency value (0.83) used here.

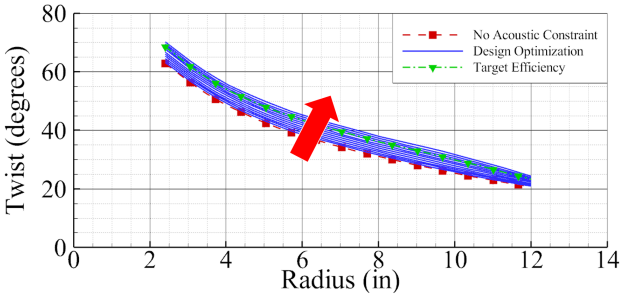

(a) Blade twist.

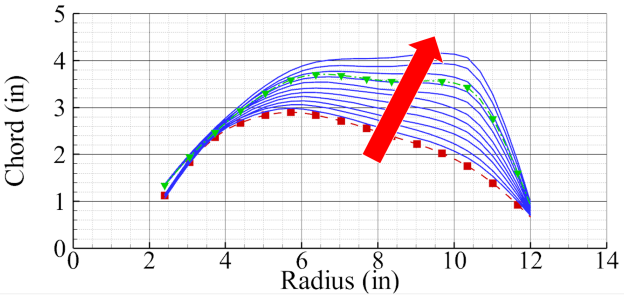

(b) Blade chord.

Figure 22: Twist and chord blade properties during proprotor design process including an A-weighted OASPL at an out-of-plane observer during a series of more restrictive acoustic constraints. Arrows indicate a more restrictive acoustic constraint.

Out of all the design optimizations, the target efficiency cases resulted in either a tonal noise dominant design or a broadband noise dominant design. Figure 23 shows a schematic of different combinations of observer position, frequency weighting, and source noise included in the computation and delineate which noise source is the dominant factor in the design. As shown in the figure:

- When the optimization only included a constraint on tonal noise, the target efficiency design was dominated by tonal noise, regardless of the frequency weighting or observer location.
- When including both tonal and broadband noise in the design optimization, when either frequency weighting or an out-of-plane observer was included in the acoustic constraint, tonal noise was the dominant factor.
- Only when both A-weighting and an out-of-plane observer were included in the acoustic constraint does broadband noise become the dominant factor.

This shows that for design optimization that includes perception, both more observer locations and frequency weighting to assess community impact should be included.

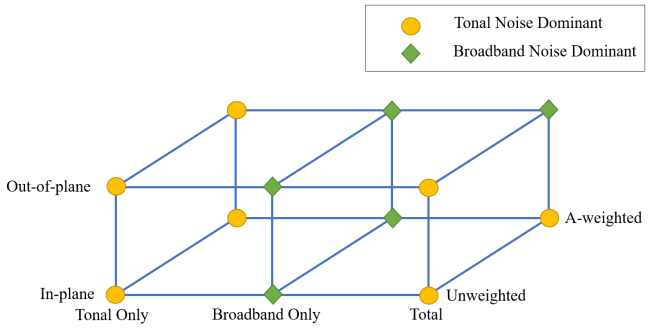

Figure 23: Source noise dominance as a result of optimization for combinations of noise source, observer position, and frequency weighting.

CONCLUSION

This paper studied the influence of observer position, frequency weighting, and broadband noise on proprotor design optimization in a forward flight configuration. It was shown that broadband noise is only influential when an out-of-plane observer position and A-weighting was included in the acoustic constraint of the design optimization. During optimizations where broadband noise was the main driver, the optimizer increases the chord on outboard sections of the blade while decreasing twist when compared to optimizations that included only tonal noise. This resulted in an increase in size of the boundary layer thickness, which resulted in a lower frequency and lower amplitude broadband noise. In addition, the tonal noise sources were significantly attenuated by both observer position and A-weighting while broadband noise was unaffected.

This paper demonstrates an important step toward a full vehicle design optimization that includes all noise sources and a perception constraint that captures community acceptance of UAM vehicles. However, many important noise sources were excluded from this current study. First, bluntness noise, which is an important component of broadband self-noise, was not included in this design. Also, important noise sources, such as installation affects, rotor-wake interaction, blade-wake interaction, and turbulence ingestion were also not included. It is unclear how these will impact the design optimization of UAM proprotors. In addition, a target efficiency of 0.83 was studied here, but the impact of tonal and broadband can be different for a higher target efficiency. Investigating these caveats will be left for future work.

ACKNOWLEDGMENTS

This work is supported by the NASA Transformational Tools and Technologies (TTT) project under the Transformative Aeronautics Concepts Program (TACP). The authors would also like to acknowledge the work of Jeremy Jones of Analytical Mechanics Associates (ASA) and Janelle Born, Venkat Iyer, and Karl Wiedemann of Analytical Services and Materials (ASM).

REFERENCES

1. Miller, C. J. and Sullivan, J. P., "Noise Constraints Effecting Optimal Propeller Designs," NASA TM 1985-86967, National Aeronautics and Space Administration, April 1985.

2. Gur, O. and Rosen, A., "Multidisciplinary Design Optimization of a Quiet Propeller," May 5–7 2008, AIAA Paper No. 2008-3073, presented at the 14th AIAA/CEAS Aeroacoustics Conference (29th AIAA Aeroacoustics Conference). doi:10.2514/6.2008-3073.

3. Pagano, A., Barbarino, M., Casalino, D., and Federico, L., "Tonal and Broadband Noise Calculations for Aeroacoustic Optimization of a Pusher Propeller," *Journal of Aircraft*, Vol. 47, No. 3, May 2010, pp. 835–848, doi:10.2514/1.45315.

4. Wisniewski, C. F., Byerley, A. R., Heiser, W., Van Treuren, K. W., and Liller, W. R., "Designing Small Propellers for Optimum Efficiency and Low Noise Footprint," June 22–26 2015, AIAA Paper No. 2015-2267, presented at the 33rd AIAA Applied Aerodynamics Conference. doi:10.2514/6.2015-2267.

5. Pullin, S., Zhou, B. Y., and Azarpeyvand, M., "Optimisation of Propellers with Noise-Based Constraints Including a Deep Learning Method for Aerofoil Prediction," June 14–17 2022, AIAA Paper No. 2022-3073, presented at the 28th AIAA/CEAS Aeroacoustics Conference (43rd AIAA Aeroacoustics Conference). doi:10.2514/6.2022-3073.

6. Zhou, B. Y., Gauger, N. R., Morelli, M., and Guardone, A., "Simulation and Sensitivity Analysis of a Wing-Tip Mounted Propeller Configuration from the Workshop for Integrated Propeller Prediction (WIPP)," June 15–19 2020, AIAA Paper No. 2020-2683, presented at the AIAA AVIATION 2020 Forum. doi:10.2514/6.2020-2683.

7. Gray, J. S., Hwang, J. T., Martins, J. R. R. A., Moore, K. T., and Naylor, B. A., "OpenMDAO: An open-source framework for multidisciplinary design, analysis, and optimization," *Structural and Multidisciplinary Optimization*, Vol. 59, No. 4, April 2019, pp. 1075–1104, doi:10.1007/s00158-019-02211-z.

8. Gill, P., Murray, W., and Saunders, M., "SNOPT: An SQP Algorithm for Large-Scale Constrained Optimizations," *SIAM Review*, Vol. 47, No. 1, March 2005, pp. 99–131, doi:10.1137/S0036144504446096.

9. Ning, A., "Using blade element momentum methods with gradient-based design optimization," *Structural and Multidisciplinary Optimization*, Vol. 64, No. 2, August 2021, pp. 991–1014, doi:10.1007/s00158-021-02883-6, https://github.com/byuflowlab/CCBlade.jl.

10. Lopes, L. V. and Burley, C. L., "ANOPP2's User's Manual," NASA TM 2016-219342, National Aeronautics and Space Administration, October 2016.

11. Wang, L., Diskin, B., Lopes, L. V., Nielsen, E. J., Lee-Rausch, E., and Biedron, R. T., "High-Fidelity AeroAcoustic Optimization Tool for Flexible Rotors," *Journal of the American Helicopter Society*, Vol. 66, No. 2, April 2021, pp. 1–16, doi:10.4050/JAHS.66.022004.

12. Ingraham, D. J., Gray, J. S., and Lopes, L. V., "Gradient-Based Propeller Optimization with Acoustic Constraints," January 7–11 2019, AIAA Paper No. 2019-1219, presented at the AIAA Scitech 2019 Forum. doi:10.2514/6.2019-1219.

13. Ingraham, D., "Design Of A Low-Noise Propeller With Low-Order Tools," *NASA Acoustics Technical Working Group*, National Aeronautics and Space Administration, April 2021.

14. Lopes, L. V., "Compact Assumption Applied to Monopole Term of Farassat's Formulations," *Journal of Aircraft*, Vol. 54, No. 5, September 2017, pp. 1649–1663, doi:10.2514/1.C034048.

15. Farassat, F., "Theory of Noise Generation from Moving Bodies with an Application to Helicopter Rotors," NASA TR R-451, National Aeronautics and Space Administration, December 1975.

16. Farassat, F., "Linear Acoustic Formulas for Calculation of Rotating Blade Noise," *AIAA Journal*, Vol. 19, No. 9, September 1981, pp. 1122–1130, doi:10.2514/3.60051.

17. Farassat, F., "Derivation of Formulations 1 and 1A of Farassat," NASA TM 2007-214853, National Aeronautics and Space Administration, March 2007.

18. Zawodny, N. S., Pettingill, N. A., Lopes, L. V., and Ingraham, D. J., "Experimental Validation of an Acoustically and Aerodynamically Optimized UAM Proprotor. Part 1: Test Setup and Results," NASA TM 2022-0015637, National Aeronautics and Space Administration, February 2023.

19. Pettingill, N. A., Zawodny, N. S., Thurman, C. S., and Lopes, L. V., "Acoustic and Performance Characteristics of an Ideally Twisted Rotor in Hover," January 11–15 & 19–21 2021, AIAA Paper No. 2021-1928, presented at the AIAA Scitech 2021 Forum. doi:10.2514/6.2021-1928.

20. Rizzi, S. A., Huff, D. L., Boyd, Jr., D. D., Bent, P., Henderson, B. S., Pascioni, K. A., Sargent, D. C., Josephson, D. L., Marsan, M., He, H., and Snider, R., "Urban Air Mobility Noise: Current Practice, Gaps, and Recommendations," NASA TP 2020-5007433, National Aeronautics and Space Administration, October 2020.

21. Silva, C. and Johnson, W., "Practical Conceptual Design of Quieter Urban VTOL Aircraft," May 10–14 2021, presented at Vertical Flight Society's 77th Annual Forum Technology Display.

22. Whiteside, S. K. S., Pollard, B. P., Antcliff, K. R., Zawodny, N. S., Fei, X., Silva, C., and Medina, G. L., "Design of a Tiltwing Concept Vehicle for Urban Air Mobility," NASA TM 2021-0017971, National Aeronautics and Space Administration, June 2021.

23. German, B. J., Ayush, J., Welstead, J. R., Whiteside, S. K. S., and Blaesser, N. J., "Design and Programmatic Overview of the Research Aircraft for eVTOL Enabling techNologies (RAVEN) Activity," June 12–16 2023, accepted for publication at the 2023 AIAA Aviation Forum and Exposition.

24. Zawodny, N. S., D. D. Boyd, J., and Nark, D. M., "Aerodynamic and Acoustic Interactions Associated with Inboard Propeller-Wing Configurations," January 11–15 & 19–21 2021, AIAA Paper No. 2021-0714, presented at AIAA Scitech 2021 Forum. doi:10.2514/6.2021-0714.

25. Hwang, J. T., "A Modular Approach to Large-Scale Design Optimization of Aerospace Systems," 2015, Ph.D. thesis, University of Michigan.

26. Lambe, A. B. and Martins, J. R. R. A., "Extensions to the design structure matrix for the description of multidisciplinary design, analysis, and optimization processes," *Structural and Multidisciplinary Optimization*, Vol. 46, 2012, pp. 273–284, doi:10.1007/s00158-012-0763-y.

27. Leishman, J. G., *Principles of helicopter aerodynamics*, Cambridge aerospace series, Cambridge University Press, Cambridge, New York, 2nd ed., 2006, OCLC: ocm61463625.

28. McDonald, R. A. and Gloudemans, J. R., "Open Vehicle Sketch Pad: An Open Source Parametric Geometry and Analysis Tool for Conceptual Aircraft Design," January 3–7 2022, AIAA Paper No. 2022-0004, presented at AIAA Scitech 2022 Forum. doi:10.2514/6.2022-0004.

29. Anderson, W. K., Biedron, R. T., Carlson, J. R., Derlaga, J. M., Druyor Jr., C. R., Gnoffo, P. A., Hammond, D. P., Jacobson, K. E., Jones, W. T., Kleb, B., Lee-Rausch, E. M., Nastac, G. C., Nielsen, E. J., Park, M. A., Rumsey, C. L., Thomas, J. L., Thompson, K. B., Walden, A. C., Wang, L., Wood, S. L., Wood, W. A., Diskin, B., Liu, Y., and Zhang, X., "FUN3D Manual: 14.0," NASA TM 2022-0017743, National Aeronautics and Space Administration, December 2022.

30. Hubbard, H. H., "Aeroacoustics of Flight Vehicles: Theory and Practice. Volume 1: Noise Sources," NASA RP 1258, WRDC TR 90-3052, National Aeronautics and Space Administration, August 1991.

31. Lopes, L. V., "ANOPP2's Farassat Formulations Internal Functional Modules (AFFIFMs) Reference Manual," NASA TM 2021-0021111, National Aeronautics and Space Administration, December 2021.

32. Gel'fand, I. M. and Shilov, G. E., *Generalized Functions: Properties and Operations*, Vol. 1, Academic Press, Inc., 11 Fifth Avenue, New York 3, New York, 1964, Translated by Eugene Saletan, Department of Physics, Northeastern University, Boston, Massachusetts.

33. Lighthill, M. J., "On Sound Generated Aerodynamically, I: General Theory," *Proceedings of the Royal Society. A, Mathematical, Physical, and Engineering Sciences*, Vol. 211, March 1952, pp. 564–587, doi:10.1098/rspa.1952.0060.

34. Lighthill, M. J., "On Sound Generated Aerodynamically, II: Turbulence as a Source of Sound," *Proceedings of the Royal Society. A, Mathematical, Physical, and Engineering Sciences*, Vol. 222, February 1954, pp. 1–32, doi:10.1098/rspa.1954.0049.

35. Ffwocs Williams, J. E. and Hawkings, D. L., "Sound Generated by Turbulence and Surfaces in Arbitrary Motion," *Philosophical Transactions of the Royal Society*, Vol. A264, No. 1151, May 1969, pp. 321–342, doi:10.1098/rsta.1969.0031.

36. Brooks, T. F., Pope, D. S., and Marcolini, M. A., "Airfoil Self-Noise and Prediction," NASA RP 1218, National Aeronautics and Space Administration, July 1989.

37. Brooks, T. F. and Burley, C. L., "Rotor Broadband Noise Prediction with Comparison to Model Data," *Journal of the American Helicopter Society*, Vol. 49, No. 1, 2004, pp. 28–42, doi:10.4050/JAHS.49.28.

38. Brooks, T. F. and Burley, C. L., "Blade Wake Interaction Noise for a Main Rotor," *Journal of the American Helicopter Society*, Vol. 49, No. 1, January 2004, pp. 11–27, doi:10.4050/JAHS.49.11.

39. Zawodny, N. A., Boyd, Jr., D. D., and Burley, C. L., "Acoustic Characterization and Prediction of Representative, Small-Scale Rotary-Wing Unmanned Aircraft System Components," May 17–19 2016, presented at AHS International 72nd Annual Forum & Technology Display.

40. Pettingill, N. A. and Zawodny, N. S., "Identification and Prediction of Broadband Noise for a Small Quadcopter," May 13–16 2019, presented at VFS International 75th Annual Forum & Technology Display.

41. Blake, J. D., Thurman, C. S., Zawodny, N. S., and Lopes, L. V., "Broadband Predictions of an Optimized Proprotor in Hover and Forward Flight," June 12–16 2023, accepted for publication at the 2023 AIAA Aviation Forum and Exposition.